Revision 3

spectroscopic evidence for the Fe^{3+} spin transition in iron-bearing δ-AlOOH at high pressure

Xiaowan Su[1], Chaoshuai Zhao[2,*], Liangxu Xu[2], Chaojia Lv[2], Xitong Song[2], Takayuki Ishii[3], Yuming Xiao[4], Paul Chow[4], Qiang Sun[1], Jin Liu[2,*]

[1]School of Earth and Space Sciences, Peking University, Beijing 100871, China.
[2]Center for High Pressure Science and Technology Advanced Research, Beijing 100094, China.
[3]Bayerisches Geoinstitut, University of Bayreuth, Bayreuth 95440, Germany.
[4]HPCAT, X-Ray Science Division, Argonne National Laboratory, Argonne, Illinois 60439, USA.

*Correspondence to: C. Zhao (chaoshuai.zhao@hpstar.ac.cn) and J. Liu (jin.liu@hpstar.ac.cn)

Highlights:

- The spin state of Fe^{3+} in δ-$(Al_{0.85}Fe_{0.15})$OOH was studied by X-ray emission spectroscopy at pressures up to 53 GPa.
- Vibrational properties of δ-$(Al_{0.85}Fe_{0.15})$OOH and δ-$(Al_{0.52}Fe_{0.48})$OOH were investigated by laser Raman spectroscopy at pressures up to 57 and 62 GPa, respectively.
- The onset pressure of the spin transition in iron-bearing δ-AlOOH increases with increasing FeOOH content.

Abstract

δ-AlOOH has emerged as a promising candidate for water storage in the lower mantle and could have delivered water into the bottom of the mantle. To date, it still remains unclear how the presence of iron affects its elastic, rheological, vibrational and transport properties, especially across the spin crossover. Here, we conducted high-pressure X-ray emission spectroscopy experiments on a δ-$(Al_{0.85}Fe_{0.15})OOH$ sample up to 53 GPa using silicone oil as the pressure transimitting medium in a diamond anvil cell. We also carried out laser Raman measurements on δ-$(Al_{0.85}Fe_{0.15})OOH$ and δ-$(Al_{0.52}Fe_{0.48})OOH$ up to 57 and 62 GPa, respectively, using neon as the pressure-transmitting medium. Evolution of Raman spectra of δ-$(Al_{0.85}Fe_{0.15})OOH$ with pressure shows two new bands at 226 and 632 cm^{-1} at 6.0 GPa, in agreement with the transition from an ordered ($P2_1nm$) to a disordered hydrogen bonding structure (*Pnnm*) for δ-AlOOH. Similarly, the two new Raman bands at 155 and 539 cm^{-1} appear in δ-$(Al_{0.52}Fe_{0.48})OOH$ between 8.5 and 15.8 GPa, indicating that the incorporation of 48 mol% FeOOH could postpone the order-disorder transition upon compression. On the other hand, the satellite peak ($K\beta'$) intensity of δ-$(Al_{0.85}Fe_{0.15})OOH$ starts to decrease at ~30 GPa and it disappears completely at 42 GPa. That is, δ-$(Al_{0.85}Fe_{0.15})OOH$ undergoes a gradual electronic spin-pairing transition at 30–42 GPa. Furthermore, the pressure dependence of Raman shifts of δ-$(Al_{0.85}Fe_{0.15})OOH$ discontinuously decreases at 32–37 GPa, suggesting that the improved hydrostaticity by the use of neon pressure medium could lead to a relatively narrow spin crossover. Notably, the pressure dependence of Raman shifts and optical color of δ-$(Al_{0.52}Fe_{0.48})OOH$ dramatically change at 41–45 GPa, suggesting that it probably undergoes a relatively sharp spin transition in the neon pressure medium. Together with literature data on the solid solutions between δ-AlOOH and ε-FeOOH, we found that the onset pressure of the spin transition in δ-(Al,Fe)OOH increases with increasing FeOOH content. These results shed new insights into the effects of iron on the structural evolution and vibrational properties of δ-AlOOH. The presence of FeOOH in δ-AlOOH can substantially influence its high-pressure behavior and stability at the deep mantle conditions and play an important role in the deep water cycle.

Keywords: Iron-bearing δ-AlOOH, spin transition, high pressure, X-ray emission spectroscopy, Raman spectroscopy

Introduction

The water cycling between the Earth's surface and interior plays a key role in the evolution and dynamics of Earth's interior (Mao and Mao, 2020; Ohira et al., 2019; Ohtani, 2005). Slab subduction and magmatism are the two key processes regulating the ingassing and outgassing rates of water and many other volatiles. Based on geochemical and petrological evidence, the amount of water entering into the mantle through subducting slabs is in the order of $(7–10)\times10^{11}$ kg/year, while water returning to the surface via magmatism is $(2–6.7)\times10^{11}$ kg/year (Ohtani, 2020). That is, $(0.3–8)\times10^{11}$ kg/year of water is likely transported into the Earth's interior. Hydrous minerals are the utmost important hosts for transporting water and hydrogen into the mantle. Thus far, most hydrous minerals (e.g., serpentine, 10Å phase, phase A, phase E) would decompose under the temperature and pressure (*P*-*T*) conditions above the topmost lower mantle. However, the pyrite-structured FeO_2Hx, the hexagonal phase (HH phase, a hexagonal ultradense hydrous phase of (Fe,Al)OOH), and δ-AlOOH phase and its solid solution with ε-FeOOH are plausibly stable under the lower-mantle *P*-*T* conditions (Ohtani (2020) and references therein). Studying the behavior of these hydrous phases at high pressure sheds light on the potential impacts of subducted hydrous materials on the structure, evolution, and geodynamics of the Earth's deep interior (Hu et al., 2020; Liu et al., 2020; Mao and Mao, 2020).

The nature of δ-AlOOH at high pressure has been extensively investigated, including crystal chemistry, phase stability, and sound velocity by both experiments and theoretical calculations (Cortona, 2017; Duan et al., 2018; Li et al., 2006; Mashino et al., 2016; Ohira et al., 2019; Tsuchiya and Tsuchiya, 2009; Tsuchiya et al., 2008). Compared to water ice, δ-AlOOH undergoes hydrogen-bond symmetrization at a relatively low pressure of ~18 GPa from neutron diffraction experiment (Sano-Furukawa et al., 2018). Additionally, recent studies by high *P*-*T* X-ray diffraction (XRD) indicate that δ-AlOOH carrying a considerable amount of water (~15 wt%) (Ohtani, 2005) could be stable down to the lowermost mantle conditions under cold subduction slabs (Duan et al., 2018; Ohira et al., 2014). That is, δ-AlOOH could be an important hydrous phase in the Earth's deep mantle and potentially delivers water down to the bottom of the mantle. Notably, δ-AlOOH exhibits sound velocities distinct from mantle ferropericlase, bridgmanite, and post-perovskite, and thus it may contribute to large low-shear-velocity

provinces (LLSVPs) and ultralow velocity zones (ULVZs) at the bottom of the lower mantle (Mashino et al., 2016).

The incorporation of FeOOH could induce profound impacts on the physical properties of δ-AlOOH in the deep mantle (e.g., spin transition, elasticity, and thermal conductivity) (Hsieh et al., 2020; Kawazoe et al., 2017; Ohira et al., 2019; Su et al., 2020). It would further affect the global geochemical cycling of ferric iron and water (hydrogen) in the deep mantle (Yuan et al., 2019; Zhang et al., 2018). It is found that iron-bearing δ-AlOOH phase, δ-$(Al_{0.824}Fe_{0.126})OOH_{1.15}$ and δ-$(Al_{0.908}Fe_{0.045})OOH_{1.14}$, exhibits elastic anomalies across the spin transition, including isothermal bulk modulus K_T, bulk sound velocity V_Φ, and the ratio of density over bulk sound velocity ρ/V_Φ (Ohira et al., 2019). Iron-bearing δ-AlOOH may thus play an important role in understanding the heterogeneous structure and composition at depths of 900–1000 km, corresponding to the spin crossover of δ-$(Al_{0.824}Fe_{0.126})OOH_{1.15}$ and δ-$(Al_{0.908}Fe_{0.045})OOH_{1.14}$ (Ohira et al., 2019). In addition, the thermal conductivity in δ-$(Al_{0.97}Fe_{0.03})OOH$, δ-$(Al_{0.88}Fe_{0.12})OOH$, and δ-$(Al_{0.85}Fe_{0.15})OOH$ vary drastically by two- to three-fold across the spin transition of Fe^{3+}. Such anomalies may contribute to a local thermal abnormal conductivity at depths approximately from 800 to 1400 km (Hsieh et al., 2020). However, most of the previous studies on δ-(Al,Fe)OOH are limited to its end-members and a low FeOOH content in δ-(Al,Fe)OOH ($0 \leqslant Fe/(Fe+Al) \leqslant 0.15$) (Duan et al., 2018; Gleason et al., 2013; Hsieh et al., 2020; Mashino et al., 2016; Ohira et al., 2019; Su et al., 2020; Zhuang et al., 2019). Knowledge of how the incorporation of Fe^{3+} affects the behavior of δ-AlOOH at high pressure is still rather scanty. Considering the significance of the spin transition of Fe^{3+} in δ-(Al,Fe)OOH, it is indispensable to study the effect of Fe^{3+} on the spin transition pressure and physical properties of δ-AlOOH.

In the present work, we synthesized a δ-$(Al_{0.85}Fe_{0.15})OOH$ (denoted as "Delta85") sample at 20 GPa and 1473 K and a δ-$(Al_{0.52}Fe_{0.48})OOH$ sample (denoted as "Delta52") at 26 GPa and 1473 K, respectively. High pressure X-ray emission (XES) experiments of the Delta85 were carried out up to 53 GPa using silicone oil as a pressure-transmitting medium in a DAC. Laser Raman spectroscopy experiments were conducted on the Delta85 and Delta52 samples up to 57 and 62 GPa, respectively, using neon as a pressure-transmitting medium. We investigated the spin transitions of the Delta85 and Delta52 at high pressure and room temperature and found

that the onset pressure of the spin transition in δ-(Al,Fe)OOH increases with increasing FeOOH concentration. These results provide new evidence for pressure-induced Fe^{3+} spin transition in δ-(Al,Fe)OOH and provide insights into how the incorporation of Fe^{3+} affects the spin transition and vibrational properties of δ-AlOOH under high pressures.

Methods

Sample synthesis and characterization

Both the Delta85 and Delta52 single-crystals were synthesized using a 1000-ton Kawai-type multi-anvil apparatus. The former was synthesized at 20 GPa and 1473 K at the Bayerisches Geoinstitut, with a mixture of Fe_2O_3 and $Al(OH)_3$ as the starting materials. The latter was synthesized at 26 GPa and 1473 K at the Institute of Physics, Chinese Academy of Sciences, using the same starting materials. The synthesis procedures followed the previous studies (Hsieh et al., 2020; Kawazoe et al., 2017; Ohira et al., 2019). The chemical compositions of the two samples were determined to be δ-$(Al_{0.85}Fe_{0.15})$OOH and δ-$(Al_{0.52}Fe_{0.48})$OOH with an uncertainty of ~1% on Al and Fe contents using a scanning electron microscope (SEM) equipped with an energy dispersive detector at Peking University (see Supplemental Materials); the measurements were conducted at an acceleration voltage of 20 kV with a current of 88 uA and a 6 μm beam size. For simplicity, the samples are hereinafter referred to as "Delta85" and "Delta52". X-ray diffraction patterns of the Delta85 and Delta52 samples are consistent with the phase with space group $P2_1nm$ under ambient conditions.

High-pressure X-ray emission spectroscopy

A symmetric diamond anvil cell (DAC) was mounted with a pair of diamond anvils with 300 μm flat culets. A Be gasket was pre-indented to ~35 μm thickness and then drilled with a 150 μm hole in the center. The synthesized Delta85 sample was loaded into the sample chamber using silicone oil as a pressure-transmitting medium. Two ruby spheres were placed next to the sample as pressure calibrant. High-pressure XES measurements were performed at 300 K at the beamline 16-IDD, Advanced Photon Source (APS), Argonne National Laboratory (ANL). The one-meter Rowland circle XES spectrometer was used to collect the decay emission X-ray

140 photons with sub-eV energy resolution. In addition, a helium tube was used to reduce scattering
141 by air. An incident X-ray beam with an energy of 11.3 keV and bandwidth of ~1 eV was used for
142 the experiments. The collection time for each XES spectrum was ~1 hour. Three to five spectra
143 were added together for good statistics at a given pressure. Pressure was determined by the
144 fluorescence of ruby and the pressure uncertainty was estimated from the pressure values
145 measured before and after collection of the XES spectra (Mao et al., 1986).
146
147 **High-pressure laser Raman spectroscopy**
148 The synthesized Delta85 and Delta52 samples were both polished to platelets of about
149 30×40 μm^2 in diameter and 10 μm in thickness. High pressure was produced by a pair of
150 diamond anvils with 300 μm flat culets. A tungsten gasket was pre-indented to 35 μm thickness
151 and then drilled with a 150 μm hole in the center. Neon gas was loaded into the sample chamber
152 as a pressure medium. Ruby spheres were placed next to the sample platelet to calibrate
153 pressure. High-pressure laser Raman spectra of the Delta85 and Delta52 phases were collected
154 using a Renishaw RM1000 Raman microscope equipped with a 250 mm spectrometer focal
155 length. The Raman signal was excited using a 532-nm wavelength diode-pumped laser (Verdi
156 V2, Coherent), delivering a maximum laser power of 20 mW focused onto an approximately 10
157 μm spot by a 20X, 0.35 (numerical aperture, NA) objective. The spectral resolution was about 2
158 cm^{-1} with a holographic diffraction grating of 1800 lines/mm. Raman spectra were collected in a
159 backscattering geometry using a Dilor XY triple spectrometer and a liquid-nitrogen-cooled CCD
160 multichannel detector. Pressure was determined by multiple measurements of the ruby
161 fluorescence before and after each experimental run (Mao et al., 1986). Raman spectra fitting
162 was carried out using the software PeakFit v4.12 with the Voigt area method.
163

164 ## Results and Discussion

165 **Spin transition of the Delta85 phase evidenced by XES**
166 XES measurements were carried out at pressures up to 53 GPa on the synthesized Delta85
167 sample (Fig. 1). The spectra are normalized to the integrated area. The Kβ emission spectrum is
168 characterized by a mainline $K\beta_{1,3}$ and a satellite line Kβ′ due to the exchange interaction

between the 3*p* core hole and the unfilled 3*d* shell. The satellite intensity is proportional to the net spin of the 3*d* shell and it thus can be considered as an indicator of the spin magnetic moment (Bergmann and Glatzel, 2009; Liu et al., 2019; Mattila et al., 2007). XES spectra of Delta85 demonstrate that the intensity of the satellite peak ($K\beta'$) initially decreases between 28.7 and 33.6 GPa, with a clear reduction by about one half at 37.9 GPa. The peak disappears completely at ~42.1 GPa, indicating that the total spin momentum of Fe^{3+} approaches to the minimum. That is, the Delta85 phase changes from the high-spin (HS) to low-spin (LS) states approximately between 30 and 42 GPa.

To further clarify the spin state of Delta85 with pressure, XES spectra at the highest pressure of 53 GPa were used as the reference for the LS state. The total spin momentum was then evaluated using the integrated spectral area from 7030 to 7048 eV with respect to that of the LS reference (Fig. 2). The spin crossover of Delta85 ranges from 30 to 42 GPa in the use of silicone oil by XES measurements, in agreement with that of 32–40 GPa from XRD data for δ-$(Al_{0.832}Fe_{0.117})OOH_{1.15}$ and 32–45 GPa from synchrotron Mössbauer spectroscopy results for δ-$(Al_{0.824}Fe_{0.126})OOH_{1.15}$ (Ohira et al., 2019). However, compared to a sharp spin crossover of 32–37 GPa from Raman results using Ne as a pressure-transmitting medium (shown in the next section), the Delta85 phase undergoes a gradual electronic spin-pairing transition under high pressures and the spin crossover is broadened likely due to the use of silicone oil as a pressure-transmitting medium. It may be related to the continuous nature of the transition (Gleason et al., 2013) and the influence of large deviatoric stress of the pressure-transmitting medium of silicone oil on the emission spectra (Klotz et al., 2009). Similar phenomena were also reported in other iron-bearing geomaterials, e.g. siderite (Mattila et al., 2007), silicate perovskite (Lin et al., 2010) and ferropericlase (Badro et al., 2003).

Laser Raman spectra of the Delta85 and Delta52 phases at high pressures

Representative Raman characteristics of the Delta85 and Delta52 phases at high pressures are shown up to 62 GPa in Figs. 3–6. In Fig. 3, nine Raman modes of Delta85 were observed in the range of 200 to 1000 cm^{-1} at ambient conditions. Two new Raman bands at 226 cm^{-1} and 632 cm^{-1} (labelled with two stars in Fig. 3) were detected at ~6.0 GPa. Meanwhile, the corresponding pressure dependence of Raman shifts of Delta85 shows clear different characteristics before and

after ~6 GPa (Fig. 4). The evidence could be assigned to the phase transition from $P2_1nm$ (ordered) to *Pnnm* (disordered), and the order-disorder transition pressure is in coincidence with that of δ-AlOOH measured using Raman spectroscopy (Mashino et al., 2016). On the other hand, the previous XRD studies suggested that δ-$(Al_{1-x}Fe_x)OOH$ ($0 \leq x \leq 0.12$) phases undergo the order-disorder phase transition at ~10 GPa (Ohira et al., 2019; Sano-Furukawa et al., 2018; Sano-Furukawa et al., 2009). This discrepancy might reflect the effect of different techniques on the detection of the phase transition of iron-bearing δ-AlOOH.

Intriguingly, the two new vibrational modes of Delta52 were observed at 8.5–15.8 GPa, including the low-frequency mode at 155 cm^{-1} and the high-frequency mode at 539 cm^{-1} (Fig. 5). The appearance of these two new codes likely corresponds to the phase transition from $P2_1nm$ (ordered) to *Pnnm* (disordered), in agreement with the previous neutron diffraction and single-crystal XRD studies on both iron-free and iron-bearing δ-AlOOH at high pressures (Furukawa et al., 2018; Sano-Furukawa et al., 2009; Ohira et al. 2019). The transition pressure was not well pinned down here due to the large pressure interval of laser Raman spectroscopic measurements. For clarity, the mean value of 12(4) GPa was illustrated by the black dashed line in Fig. 6. The order-disorder transition of hydrogen bond in δ-(Al,Fe)OOH may serve as a precursor of hydrogen-bond symmetrization and it plays a key role in understanding the physical properties of δ-(Al,Fe)OOH under high pressures (Ohira et al., 2019; Sano-Furukawa et al., 2018). Moreover, Thompson et al. (2020) recently demonstrated the occurrence of phase transition from $P2_1nm$ (ordered) to *Pnnm* (disordered) in ε-FeOOH at ~18 GPa via XRD, Fourier transform infrared spectroscopy, and optical absorption methods. Therefore, it seems that the phase transition pressure from $P2_1nm$ (ordered-hydrogen bond) to *Pnnm* (disordered-hydrogen bond) increases with increasing FeOOH content for ε-$(Al_{1-x}Fe_x)OOH$ ($0.52 \leq x \leq 1$).

Furthermore, the hydrogen-bond symmetrization of δ-AlOOH was reported at ~18 GPa according to neutron diffraction experiments (Sano-Furukawa et al., 2018). Meanwhile, theoretical calculations predicted the hydrogen-bond symmetrization at 30 GPa for δ-AlOOH (Tsuchiya et al., 2008). It is noted that the Raman spectra of δ-AlOOH calculated by Tsuchiya et al. (2008) displayed a large discontinuity in Raman shifts across the hydrogen-bond

symmetrization. On the other hand, the onset pressure of hydrogen-bond symmetrization in ε-FeOOH was theoretically predicted to range approximately from 10 to 43 GPa (Gleason et al., 2013; Ohira et al., 2019; Thompson et al., 2017). Recently, Thompson et al. (2020) suggested that the onset pressure of hydrogen-bond symmetrization in ε-FeOOH might be at ~18 GPa based on the results of XRD and Fourier transform infrared spectroscopy measurements. That is, the transition pressure of the hydrogen-bond symmetrization might be independent of the FeOOH content of δ-(Al,Fe)OOH. We note that there is an abrupt decrease in the Raman mode at ~804 cm^{-1} of the Delta85 phase at ~20 GPa (Fig. 4). This behavior might be interpreted by the hydrogen-bond symmetrization. However, a similar phenomenon and other abnormal changes were not evidently observed in the Delta52 phase at 16–41 GPa. It is possibly due to the high FeOOH content in Delta52, causing the relatively weak Raman signals at 700–900 cm^{-1}. Further work is needed to clarify how the incorporation of FeOOH affects the hydrogen-bond symmetrization of δ-AlOOH.

Regarding the spin transition of Fe^{3+} in δ-$(Al_{0.85}Fe_{0.15})$OOH, we observed three Raman modes approximately at 481, 756, 804 cm^{-1} discontinuously decreasing at 32–37 GPa with the use of neon as a pressure-transmitting medium (Fig. 4). By comparison, Raman spectroscopic features of the Delta52 phase change significantly at 41–45 GPa (Figs. 5 and 6). This may be associated with the spin transition of Fe^{3+} in δ-(Al,Fe)OOH (Hsieh et al., 2020; Ohira et al., 2019). In the pressure range of 41–45 GPa, the three Raman modes below 700 cm^{-1} of Delta52 jump to higher wavenumbers while a splitting mode at 782 cm^{-1} shifts to lower wavenumbers. These properties may serve as a diagnostic signature of the spin transition of Fe^{3+} in Delta52, comparable to that in siderite (Lin et al., 2012). At the same time, the color of the Delta52 sample is semitransparent brown at the HS state below 41 GPa (Fig. 5). The inset shows optical microscope images of the single-crystal Delta52 samples in the DAC. The color of the sample changes from semitransparent brown to nontransparent with high opacity at 45 GPa. A similar phenomenon was also observed in ε-FeOOH and siderite across the spin transition (Lavina et al., 2009; Lobanov et al., 2015; Thompson et al., 2020). The color of ε-FeOOH is translucent orange at the HS state, but reddened with increasing pressure and becomes opaque at 45 GPa due to the spin transition of Fe^{3+} (Thompson et al., 2020). The change of crystal color can be assigned to a significant increase in the overall optical absorption of Delta52 and ε-FeOOH at the LS state

(Thompson et al., 2020).

Vibrational properties of the Delta85 and Delta52 phases

The pressure dependence of Raman shifts was fitted linearly within the pressure range of the $P2_1nm$, *Pnnm*-HS, and *Pnnm*-LS structures, respectively, for the Delta85 and Delta52 phases (Figs. 4 and 6, Tables 1–2). In the case of the vibrational properties of Delta52, at frequencies below 400 cm^{-1}, the pressure-induced Raman shifts *dv/dP* of the three modes at 145, 243, and 339 cm^{-1} (at ambient conditions) range from 3.38–8.16 cm^{-1}/GPa in $P2_1nm$ below ~10 GPa. The corresponding slopes (*dv/dP*) are 0.88–1.01 cm^{-1}/GPa in *Pnnm* at 16–41 GPa. Meanwhile, Kagi et al. (2010) reported a similar phenomenon from infrared spectra measurements of δ-AlOOH and δ-AlOOD. They observed a drastic decrease in the pressure-response absorption bands at 1180 and 1330 cm^{-1} at ~10 GPa. On the contrary, the pressure dependence of Raman mode (*dv/dP*) at 418 cm^{-1} (at ambient conditions) is 0.19 cm^{-1}/GPa in $P2_1nm$, while the corresponding slope value is 1.99 cm^{-1}/GPa in *Pnnm* at the high spin state. The drastic changes in the pressure dependence of Raman modes at ~10 GPa likely indicate the phase transition from $P2_1nm$ to *Pnnm* (Ohira et al., 2019; Sano-Furukawa et al., 2018). We note that the low-frequency Raman modes (below 400 cm^{-1}) move faster than the high-frequency modes (above 400 cm^{-1}) for the Delta52 phase in $P2_1nm$. Intriguingly, this trend is reversed with the high-frequency modes moving faster for the Delta52 phase in *Pnnm*. This is consistent with the characteristics of normalized lattice parameters as reported by XRD experiments in δ-AlOOH from $P2_1nm$ to *Pnnm* (Ohira et al., 2019; Sano-Furukawa et al., 2009).

The low-frequency modes of Delta52 become much stiffener across the spin transition, with the corresponding Raman frequency increasing slowly with pressure at the LS state. The pressure dependence of Raman modes (*dv/dP*) at 155 cm^{-1} (at 15.8 GPa) dramatically decreases from 1.01 to 0.20 cm^{-1}/GPa and that at 420 cm^{-1} reduces from 1.99 to 0.68 cm^{-1}/GPa from the HS to LS states. By contrast, the high-frequency modes become much softener and the pressure dependences are largely enhanced at the LS state. The mode at 539 cm^{-1} significantly increases from 2.25 to 3.52 cm^{-1}/GPa throughout the spin crossover. Those results indicate that the *Pnnm* phase exhibits vibrational properties distinct between the HS and LS states.

Combined with XRD and Raman results from previous studies and this work, the mode

Grüneisen parameters (γ_i) were derived as follows:

$$\gamma_i = -\frac{d\ln\nu_i}{d\ln V} = \frac{K_T}{\nu}\left(\frac{d\nu_i}{dP}\right) \quad (1)$$

where ν_0, V, P, and K_T are frequency at ambient conditions in cm^{-1}, volume in $Å^3$, pressure in GPa and isothermal bulk modulus in GPa, respectively. The K_0 values (see notes in Table 2) derived from the equation of state (EoS) of Delta52 was used to calculate these mode Grüneisen parameters (γ_i). Regarding the Delta52 phase in $P2_1nm$, the γ_i values are 3.13, 4.49 and 1.75 below 400 cm^{-1} and 0.06, 0.71 and 0.59 above 400 cm^{-1}. Notably, the major contribution to the thermodynamic Grüneisen parameters γ_i is from the low-frequency modes as reported in carbonates (Liu et al., 2016; Williams et al., 1992). Moreover, the mode Grüneisen parameters γ_i dramatically change across the phase transition from $P2_1nm$ to $Pnnm$ and from the HS to LS state, respectively, in the Delta52 phase (Table 2).

The effect of FeOOH content on the spin transition of δ-(Al,Fe)OOH

In this study, we obtained the spin transition pressure of the Delta85 phase between 30 to 42 GPa via XES experiments using silicone oil as a pressure-transmitting medium and between 32 to 37 GPa via Raman experiments using neon. These results are in agreement with the spin crossover of δ-$(Al_{0.908}Fe_{0.047})OOH_{1.14}$ and δ-$(Al_{0.832}Fe_{0.117})OOH_{1.15}$ by XRD studies and with that of δ-$(Al_{0.824}{}^{57}Fe_{0.126})OOH_{1.15}$ by synchrotron Mössbauer spectroscopy experiments (Ohira et al., 2019). Meanwhile, utilizing time-domain thermoreflectance (TDTR), Hsieh et al. (2020) reported the spin transition of δ-$(Al_{0.97}Fe_{0.03})OOH$, δ-$(Al_{0.88}Fe_{0.12})OOH$, and δ-$(Al_{0.85}Fe_{0.15})OOH$ at 30–45 GPa and 300 K based on their lattice thermal conductivity anomalies. The width of spin transition reported by Hsieh et al. (2020) is slightly broader than those reported in this study and Ohira et al. (2019). It might be overestimated due to the relatively large uncertainty of ~30% in the lattice thermal conductivity anomalies with increasing pressure. On the other hand, the spin transition pressure of the Delta52 phase is between 41 and 45 GPa via the laser Raman experiment using neon as a pressure-transmitting medium in this study. The spin crossover of Delta52 is 3–5 GPa lower than that of ε-FeOOH by XRD experiments using the same pressure-transmitting medium (Thompson et al., 2020; Zhuang et al., 2019). It should be mentioned that Gleason et al. (2013) reported that the spin crossover of ε-FeOOH is much wider

317 from 40 to 65 GPa through theoretical calculations and XES experiments without any
318 pressure-transmitting media. It is likely to be associated with the large deviatoric stress in the
319 sample chamber for their XES measurements on ε-FeOOH.

320 The FeOOH content dependence of the spin transition pressure of δ-(Al,Fe)OOH was
321 summarized in Fig. 7 and Table 3. The onset pressure of the spin transition in iron-bearing
322 δ-AlOOH increases with increasing FeOOH content. The results were linearly fitted for those
323 experiments with the only use of helium or neon as a pressure-transmitting medium in order to
324 eliminate the influence of large deviatoric stress on the spin transition pressure. For
325 δ-(Al,Fe)OOH, the Fe/(Fe+Al) ratio dependence of the spin transition pressure was as follows:

326 $$P_{ST}(GPa) = 34.9(\pm 4) \quad 11.6(\pm 1.6)\,\chi_{Fe} \qquad (2)$$

327 where subscript *ST* is an abbreviation of spin transition, χ_{Fe} represents the FeOOH content of
328 δ-(Al,Fe)OOH in the unit of mol%. These results suggest that the mixed spin transition state
329 would be stabilized to higher pressures with increasing FeOOH concentration. The positive
330 correlation between iron content and spin transition pressure has also been reported for
331 (Mg,Fe)O (Fei et al., 2007; Lin et al., 2005). We note that the spin transition pressure
332 significantly increases with increasing FeO content, from 40 GPa for $(Mg_{0.80}Fe_{0.20})O$ to 80 GPa
333 for $(Mg_{0.42}Fe_{0.58})O$, due to strong interactions between ferrous ion in (Mg,Fe)O (Fei et al., 2007).
334 The spin transition pressure of $(Mg,Fe)CO_3$, by contrast, appears not to change with varying
335 ferrous ion concentrations, due to weak interactions between ferrous ions that are distantly
336 isolated by CO_3^{2-} units (Liu et al., 2014). Considering the onset pressure and width of the spin
337 crossover with varying FeOOH content, δ-(Al,Fe)OOH may exhibit moderate interactions
338 among adjacent iron atoms, compared to (Mg,Fe)O and $(Mg,Fe)CO_3$.
339

340 ## Implications

341 The spin crossover of the Delta85 phase was evidenced between 30 and 42 GPa at 300 K by
342 XES experiments and 32 to 37 GPa by Raman experiments. With adding more FeOOH into
343 δ-AlOOH, the spin transition pressure of Fe^{3+} in the Delta52 phase increases to 41–45 GPa on
344 the basis of laser Raman spectroscopy measurements. Together with the previous studies on
345 δ-(Al,Fe)OOH (including ε-FeOOH), we infer that the spin transition pressure of δ-(Al,Fe)OOH

346 slowly increases with increasing FeOOH content (Gleason et al., 2013; Hsieh et al., 2020; Ohira
347 et al., 2019; Thompson et al., 2020; Zhuang et al., 2019). It has been proposed that ferropericlase
348 (Mg,Fe)O and ferromagnesite (Mg,Fe)CO_3 would uptake more iron when entering the low spin
349 state in the lower mantle (Cerantola et al., 2017; Lobanov et al., 2015). Similarly, δ-(Al,Fe)OOH
350 may also become more enriched in FeOOH across the spin transition of iron at the middle
351 mantle conditions. Moreover, the presence of FeOOH and spin transition substantially alter the
352 physical properties of iron-bearing δ-AlOOH, e.g., isothermal bulk modulus (K_T), bulk sound
353 velocity (V_Φ), and thermal conductivity (κ). Such anomalies may potentially contribute to the
354 profile of seismic velocities and thermal state of the deep mantle at depths of ~900–1300 km
355 (Hsieh et al., 2020; Ohira et al., 2019). Furthermore, a hexagonal ultradense hydrous phase,
356 (Al,Fe)OOH with 20-40 mol% Al was discovered in laser-heated X-ray diffraction experiments
357 and stabilized at 107–136 GPa and 2400 K (Zhang et al., 2018). Meanwhile, iron-bearing
358 AlOOH was found to coexist with bridgmanite at 104–126 GPa and 1750–2500 K, indicating
359 that it is a promising candidate hydrous phase in the deep mantle (Yuan et al., 2019). Therefore,
360 it may deliver water down to the bottom of the mantle and extend the deep water cycle
361 throughout the whole mantle (Duan et al., 2018; Kawazoe et al., 2017; Sano et al., 2008; Yuan et
362 al., 2019). If iron-bearing δ-AlOOH accumulates at the lowermost mantle via cold subducting
363 oceanic slabs, it likely dehydrates near the core-mantle boundary due to the steep increase in
364 temperature with depth (Yuan et al., 2019). The released water would react with iron-rich
365 materials and/or iron to generate hydrogen-bearing iron peroxide patches, accounting for seismic
366 features observed in ULVZs (Hu et al., 2020; Liu et al., 2017). Those processes would impact
367 the structure, evolution, and geodynamics of the Earth's deep interior.
368

Acknowledgments

We acknowledge H. Tang for providing technical support on sample synthesis, Y. Zhang and B. Wang for experimental assistance, and P. Dera for constructive discussions. This study is funded by the National Key Research and Development Program of China (2019YFA0708502). J. Liu acknowledges support from the National Natural Science Foundation of China (NSFC Grant no. U1930401). Part of this work was performed at HPCAT (Sector 16), Advanced Photon Source (APS), Argonne National Laboratory. HPCAT operations are supported by DOE-NNSA's Office of Experimental Sciences. The Advanced Photon Source is a U.S. Department of Energy (DOE) Office of Science User Facility operated for the DOE Office of Science by Argonne National Laboratory under Contract No. DE-AC02-06CH11357.

Figure captions

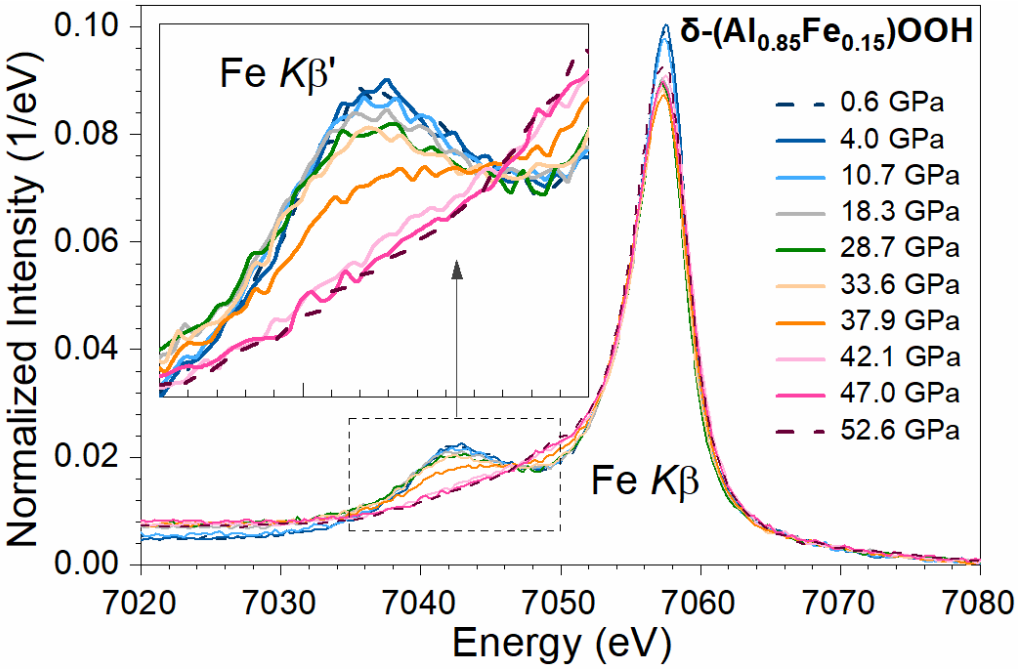

Figure 1. High-pressure X-ray emission Fe-*K*β spectra of δ-$(Al_{0.85}Fe_{0.15})OOH$ at 300 K. The integrated intensity of the XES spectra was normalized to the same area at 7018–7083 eV. Inset: the satellite emission peak (*K*β′) between 7034 and 7050 eV. The changes of the satellite peak intensity are attributed to the HS to LS transition in Fe^{3+} of δ-$(Al_{0.85}Fe_{0.15})OOH$. The disappearance of the satellite peak has been used as a robust criterion for the electronic spin-pairing transition of iron in other iron-bearing phases, e.g. ferropericlase (Badro et al., 2003) siderite (Mattila et al., 2007), and hydrogen-bearing FeO_2 (Liu et al., 2019).

This is the peer-reviewed, final accepted version for American Mineralogist, published by the Mineralogical Society of America.
The published version is subject to change. Cite as Authors (Year) Title. American Mineralogist, in press.
DOI: https://doi.org/10.2138/am-2021-7541. http://www.minsocam.org/

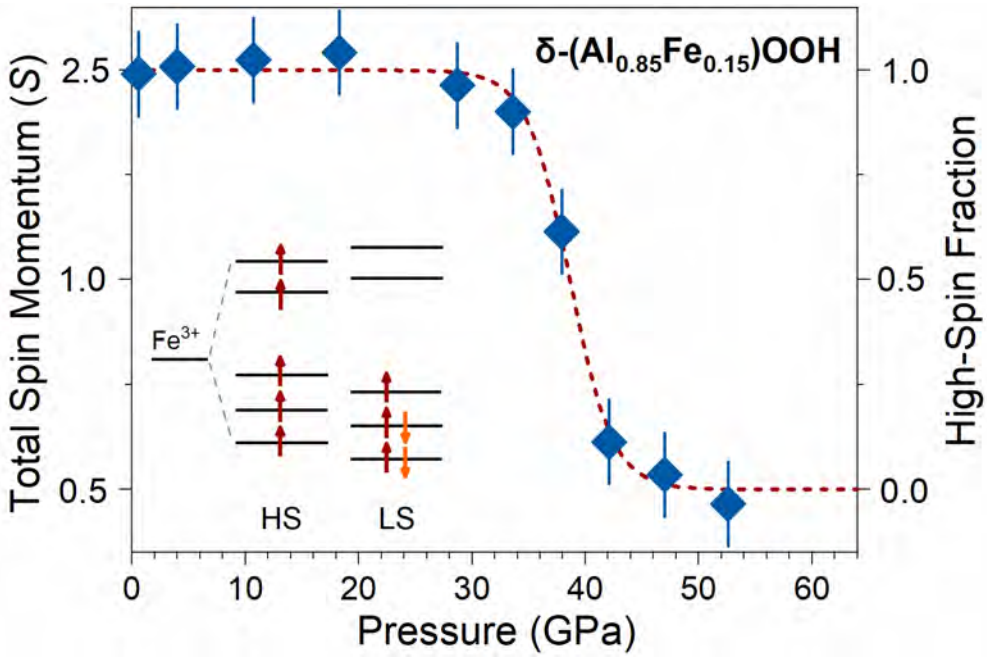

Figure 2. Pressure-induced spin transition of Fe^{3+} in the δ-$(Al_{0.85}Fe_{0.15})OOH$ phase. Total spin momentum and HS fraction of δ-$(Al_{0.85}Fe_{0.15})OOH$ as a function of pressure derived from the XES measurements at 300 K.

This is the peer-reviewed, final accepted version for American Mineralogist, published by the Mineralogical Society of America.
The published version is subject to change. Cite as Authors (Year) Title. American Mineralogist, in press.
DOI: https://doi.org/10.2138/am-2021-7541. http://www.minsocam.org/

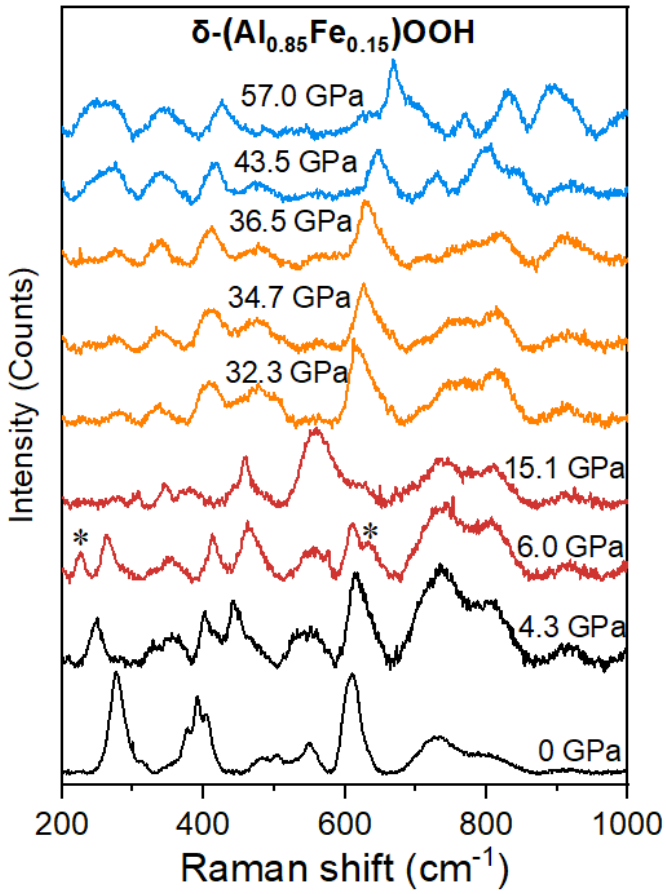

Figure 3. Representative Raman spectra of δ-$(Al_{0.85}Fe_{0.15})OOH$ as a function of pressure at 300 K. The star symbols represent the two new Raman bands at 226 cm^{-1} and 632 cm^{-1} at ~6.0 GPa. The black, red, orange, and blue colors denote $P2_1nm$ and $Pnnm$ at the high, mixed, and low spin states, respectively. Neon was used as a pressure-transmitting medium.

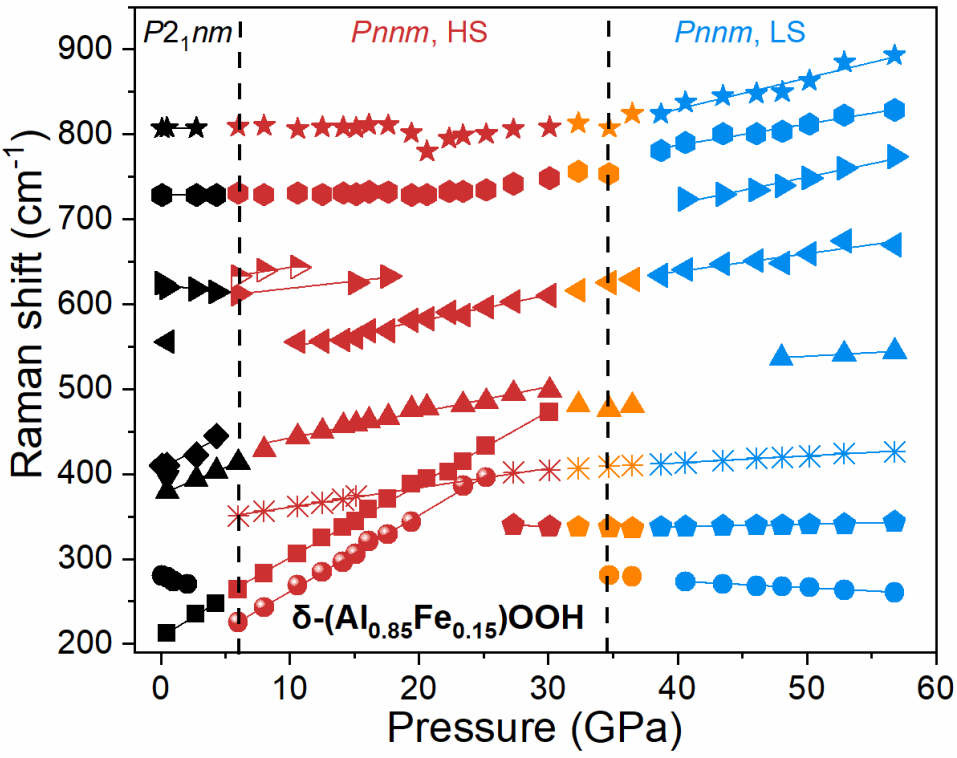

405

406 **Figure 4.** Raman shifts of δ-$(Al_{0.85}Fe_{0.15})OOH$ as a function of pressure at 300 K. The black
407 dashed line at ~6 GPa could be assigned to the phase transition from *P*2_1*nm* (ordered) to *Pnnm*
408 (disordered) (Ohira et al., 2019). The transition pressure is in coincidence with that of δ-AlOOH
409 obtained using Raman spectroscopy (Mashino et al., 2016). Interestingly, an abrupt decrease of
410 Raman mode at ~804 cm^{-1} softens at ~20 GPa. It might be related to the hydrogen-bond
411 symmetrization in δ-$(Al_{0.85}Fe_{0.15})OOH$. Meanwhile, the three Raman modes at ~481, 756, 804
412 cm^{-1} discontinuously decrease at 32–37 GPa, suggesting the spin transition of Fe^{3+} in
413 δ-$(Al_{0.85}Fe_{0.15})OOH$ (shown as the black dashed line at ~34.7 GPa). Black, red, orange, and blue
414 symbols represent Raman shifts in *P*2_1*nm* and *Pnnm* at the high, mixed, and low spin states,
415 respectively.

416

This is the peer-reviewed, final accepted version for American Mineralogist, published by the Mineralogical Society of America.
The published version is subject to change. Cite as Authors (Year) Title. American Mineralogist, in press.
DOI: https://doi.org/10.2138/am-2021-7541. http://www.minsocam.org/

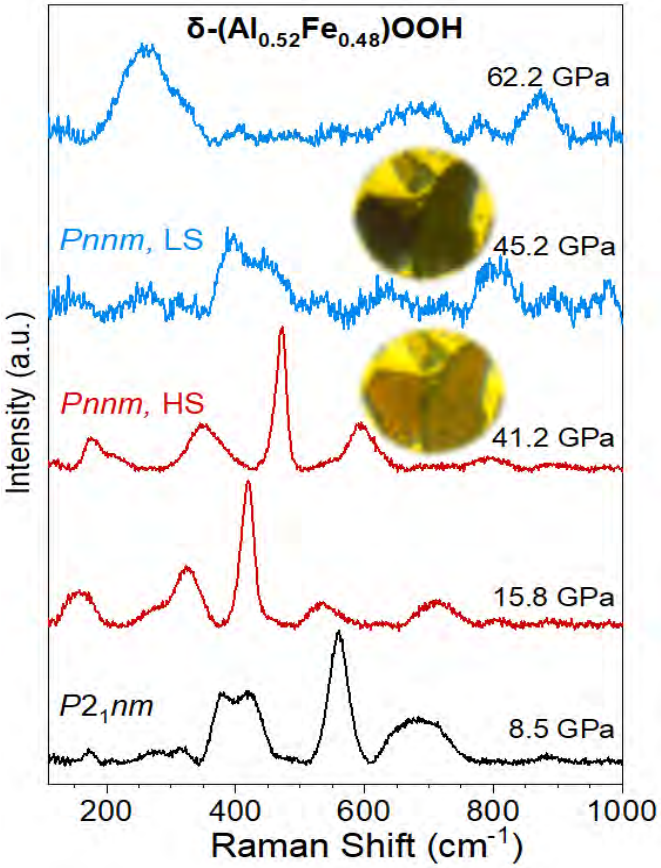

Figure 5. Representative Raman spectra of δ-$(Al_{0.52}Fe_{0.48})OOH$ phase as a function of pressure at room temperature. The dramatic change in Raman modes from 41.2 to 45.2 GPa likely indicates the occurrence of the spin transition of Fe^{3+} in δ-$(Al_{0.52}Fe_{0.48})OOH$. Insets: the color evolution of δ-$(Al_{0.52}Fe_{0.48})OOH$ sample was captured through optical microscope images with a diameter of ~50 μm. A tiny piece of Au was atop δ-$(Al_{0.52}Fe_{0.48})OOH$ samples. Neon was used as a pressure-transmitting medium.

This is the peer-reviewed, final accepted version for American Mineralogist, published by the Mineralogical Society of America.
The published version is subject to change. Cite as Authors (Year) Title. American Mineralogist, in press.
DOI: https://doi.org/10.2138/am-2021-7541. http://www.minsocam.org/

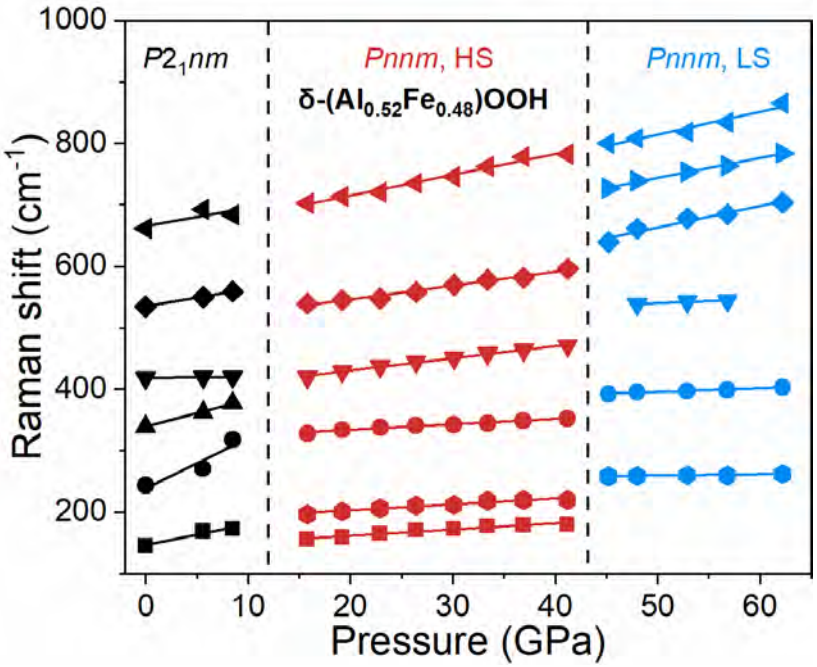

Figure 6. Raman shifts of δ-$(Al_{0.52}Fe_{0.48})OOH$ phase as a function of pressure. Black, red, and blue symbols correspond to space groups of $P2_1nm$, *Pnnm*-HS, and *Pnnm*-LS, respectively. The dashed line at ~12(4) GPa represents the order-disorder transition from $P2_1nm$ to *Pnnm*-HS (Ohira et al., 2019; Sano-Furukawa et al., 2018), while the line at ~43 GPa indicates the spin transition of δ-$(Al_{0.52}Fe_{0.48})OOH$. Neon was used as a pressure-transmitting medium.

This is the peer-reviewed, final accepted version for American Mineralogist, published by the Mineralogical Society of America.
The published version is subject to change. Cite as Authors (Year) Title. American Mineralogist, in press.
DOI: https://doi.org/10.2138/am-2021-7541. http://www.minsocam.org/

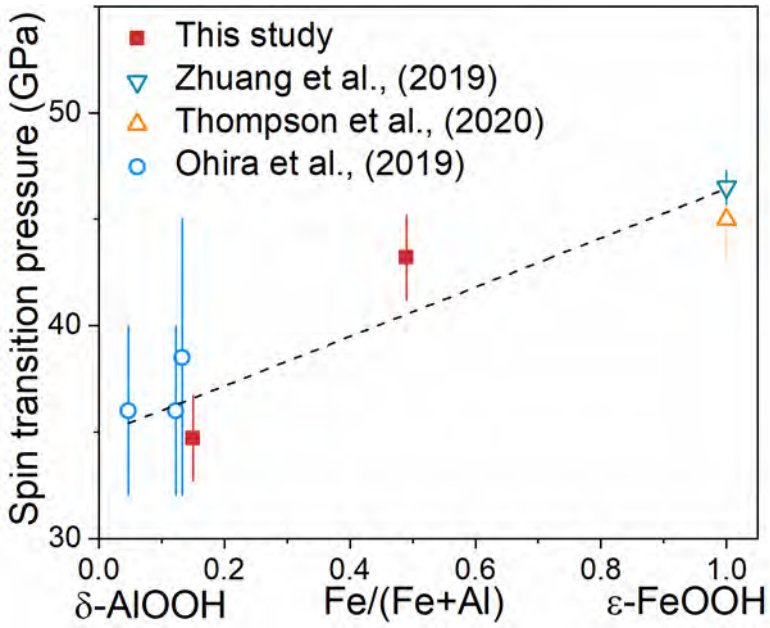

Figure 7. The spin transition pressure of δ-(Al,Fe)OOH as a function of the Fe/(Fe+Al) ratio under quasi-hydrostatic conditions. Solid red squares: δ-$(Al_{0.85}Fe_{0.15})OOH$ and δ-$(Al_{0.52}Fe_{0.48})OOH$ with neon as a pressure-transmitting medium, this study; open blue circles: δ-$(Al_{0.908}Fe_{0.045})OOH_{1.14}$, δ-$(Al_{0.832}Fe_{0.117})OOH_{1.15}$ and δ-$(Al_{0.824}Fe_{0.126})OOH_{1.15}$ with helium as a pressure-transmitting medium, Ohira et al. (2019); open cyan up triangles: ε-FeOOH with neon as a pressure-transmitting medium, Thompson et al. (2020); open cyan down triangles: ε-FeOOH with neon as a pressure-transmitting medium, Zhuang et al. (2019). The error bar represents the spin transition pressure range of individual composition. The dotted line is a linear fit to the spin transition pressures of δ-(Al,Fe)OOH. Note that the datasets of δ-(Al,Fe)OOH under non-hydrostatic pressure-transmitting media or by theoretical calculations are not included in the fitting.

447 Table 1. Experimental vibrational parameters of δ-$(Al_{0.85}Fe_{0.15})OOH$ at high pressures

$P2_1nm$[a]			*Pnnm*-HS[b]			*Pnnm*-LS[c]		
v_i[d]	dv_i/dP	γ_i	v_i[d]	dv_i/dP	γ_i	v_i[d]	dv_i/dP	γ_i
212	9.36(72)	6.49(50)	226	9.00(14)	6.17(10)	273	-0.95(6)	-0.84(5)
278	-4.96(82)	-2.62(43)	264	8.61(13)	5.06(8)	338	0.29(2)	0.21(1)
378	6.21(15)	2.42(6)	350	2.19(8)	0.97(4)	413	0.82(2)	0.48(1)
404	8.02(154)	2.92(56)	413	3.02(16)	1.13(6)	533	0.85(1)	-
610	-1.85(37)	-0.45(9)	537[e]	3.05(13)	0.88(4)	641	2.17(20)	0.82(8)
			612	1.68(27)	0.43(7)	723	3.14(22)	1.05(7)
			633	2.42(54)	0.59(13)	790	3.05(32)	0.93(10)
						837	3.58(26)	1.03(7)

448 [a] $P2_1nm$, 0–5 GPa, K_{T0} = 147 GPa, K_T' = 4 (Ohira et al., 2019);

449 [b] *Pnnm*-HS, 5–32 GPa, K_{T0} = 155 GPa, K_T' = 8 (Ohira et al., 2019);

450 [c] *Pnnm*-LS, 37–57 GPa, K_{T0} = 241 GPa, K_T' = 4 (Ohira et al., 2019);

451 [d] The measured initial frequencies v_i of Raman modes are from $P2_1nm$, *Pnnm*-HS, and *Pnnm*-LS structures of
452 δ-$(Al_{0.52}Fe_{0.48})OOH$ at 0, 6.0 and 43.5 GPa, respectively. These modes are used to derive the mode Grüneisen
453 parameters γ_i. v_i in the unit of cm^{-1}; dv_i/dP in the unit of cm^{-1}/GPa.

454 [e] This mode was derived from a linear fit in the corresponding pressure range.

455

456 **Table 2.** Experimental vibrational parameters of δ-$(Al_{0.52}Fe_{0.48})OOH$ at high pressures

$P2_1nm$[a]			*Pnnm*-HS[b]			*Pnnm*-LS[c]		
v_i[d]	dv_i/dP	γ_i	v_i[d]	dv_i/dP	γ_i	v_i[d]	dv_i/dP	γ_i
145	3.38(70)	3.13(65)	155	1.01(10)	1.41(13)	259	0.20(4)	0.18(4)
243	8.2(29)	4.49(16)	197	0.96(10)	1.05(11)	395	0.59(6)	0.35(4)
339	4.42(26)	1.75(10)	328	0.88(5)	0.58(4)	538	0.68(6)	0.30(3)
418	0.19(3)	0.06(1)	420	1.99(6)	1.02(3)	661	3.52(43)	1.24(15)
535	2.85(6)	0.71(2)	539	2.25(12)	0.90(5)	739	3.25(13)	1.03(4)
662	2.9(21)	0.59(43)	703	3.38(18)	1.04(5)	808	3.71(47)	1.07(13)

457 [a] $P2_1nm$, 0–10 GPa, K_{T0} = 134 GPa, K_T' = 4.04;

458 [b] *Pnnm*-HS, 10–42 GPa, K_{T0} = 216 GPa, K_T' = 3.98;

459 [c] *Pnnm*-LS, 45–62 GPa, K_{T0} = 234 GPa, K_T' = 4.0;

460 [d] The measured initial frequencies v_i of Raman modes are from $P2_1nm$, *Pnnm*-HS, and *Pnnm*-LS structures of
461 δ-$(Al_{0.52}Fe_{0.48})OOH$ at 0, 15.8 and 48 GPa, respectively. These modes are used to derive the mode Grüneisen
462 parameters γ_i, respectively. v_i in the unit of cm^{-1}; dv_i/dP in the unit of cm^{-1}/GPa.

463

464 **Table 3.** Pressure ranges of the spin transition of Fe^{3+} in δ-(Al,Fe)OOH at room temperature.

Composition	Method	PTM[a]	Spin crossover (GPa)	Reference
δ-$(Al_{0.85}Fe_{0.15})OOH$	XES[b]	Silicone oil	30–42	This study
δ-$(Al_{0.85}Fe_{0.15})OOH$	Raman	Ne	32–37	This study
δ-$(Al_{0.52}Fe_{0.48})OOH$	Raman	Ne	41–45	This study
δ-$(Al_{0.908}Fe_{0.045})OOH_{1.14}$	XRD[c]	Ne	32–40	Ohira et al. (2019)
δ-$(Al_{0.832}Fe_{0.117})OOH_{1.15}$	XRD	He	32–40	Ohira et al. (2019)
δ-$(Al_{0.824}Fe_{0.126})OOH_{1.15}$	MS[d]	He	32–45	Ohira et al. (2019)
δ-$(Al_{0.97}Fe_{0.03})OOH$	TDTR[e]	Silicone oil	30–45	Hsieh et al. (2020)
δ-$(Al_{0.88}Fe_{0.12})OOH$	TDTR	Silicone oil	30–45	Hsieh et al. (2020)
δ-$(Al_{0.85}Fe_{0.15})OOH$	TDTR	Silicone oil	30–45	Hsieh et al. (2020)
ε-FeOOH	XES	None	40–60	Gleason et al. (2013)
ε-FeOOH	XRD	None	46–51	Gleason et al. (2013)
ε-FeOOH	DFT[f]	-	43–65	Gleason et al. (2013)
ε-FeOOH	XRD	Ne	~45(2)	Thompson et al. (2020)
ε-FeOOH	FTIR[g]	KBr	~45(2)	Thompson et al. (2020)
ε-FeOOH	XRD	Ne	45–47	Zhuang et al. (2019)
ε-FeOOH	XRD	None	41–43	Zhuang et al. (2019)

465 [a] PTM: pressure-transmitting medium;
466 [b] XES: X-ray emission spectroscopy;
467 [c] XRD: X-ray diffraction;
468 [d] MS: Mössbauer spectroscopy;
469 [e] TDTR: time-domain thermoreflectance;
470 [f] DFT: Density function theory;
471 [g] FTIR: Fourier transform infrared spectroscopy.

References

Badro, J., Fiquet, G., Guyot, F., Rueff, J.P., Struzhkin, V.V., Vanko, G., and Monaco, G. (2003) Iron partitioning in Earth's mantle: toward a deep lower mantle discontinuity. Science, 300(5620), 789-91.

Bergmann, U., and Glatzel, P. (2009) X-ray emission spectroscopy. Photosynth Research, 102(2-3), 255-66.

Cerantola, V., Bykova, E., Kupenko, I., Merlini, M., Ismailova, L., McCammon, C., Bykov, M., Chumakov, A.I., Petitgirard, S., Kantor, I., Svitlyk, V., Jacobs, J., Hanfland, M., Mezouar, M., Prescher, C., Ruffer, R., Prakapenka, V.B., and Dubrovinsky, L. (2017) Stability of iron-bearing carbonates in the deep Earth's interior. Nature Communications, 8, 15960.

Cortona, P. (2017) Hydrogen bond symmetrization and elastic constants under pressure of delta-AlOOH. Journal of Physics: Condensed Matter, 29(32), 325505.

Duan, Y., Sun, N., Wang, S., Li, X., Guo, X., Ni, H., Prakapenka, V.B., and Mao, Z. (2018) Phase stability and thermal equation of state of δ-AlOOH: Implication for water transportation to the Deep Lower Mantle. Earth and Planetary Science Letters, 494, 92-98.

Fei, Y., Zhang, L., Corgne, A., Watson, H., Ricolleau, A., Meng, Y., and Prakapenka, V. (2007) Spin transition and equations of state of (Mg, Fe)O solid solutions. Geophysical Research Letters, 34(17), L17307.

Gleason, A.E., Quiroga, C.E., Suzuki, A., Pentcheva, R., and Mao, W.L. (2013) Symmetrization driven spin transition in ε-FeOOH at high pressure. Earth and Planetary Science Letters, 379, 49-55.

Hsieh, W.P., Ishii, T., Chao, K.H., Tsuchiya, J., Deschamps, F., and Ohtani, E. (2020) Spin transition of iron in δ-(Al,Fe)OOH induces thermal anomalies in Earth's lower mantle. Geophysical Research Letters, e2020GL087036.

Hu, Q., Liu, J., Chen, J., Yan, B., Meng, Y., Prakapenka, V.B., Mao, W.L., and Mao, H.-K. (2020) Mineralogy of the deep lower mantle in the presence of H_2O, National Science Review, in press.

Kagi, H., Ushijima, D., Sano-Furukawa, A., Komatsu, K., Iizuka, R., Nagai, T., and Nakano, S. (2010) Infrared absorption spectra of δ-AlOOH and its deuteride at high pressure and implication to pressure response of the hydrogen bonds. Journal of Physics: Conference Series, 215, 012052.

Kawazoe, T., Ohira, I., Ishii, T., Ballaran, T.B., McCammon, C., Suzuki, A., and Ohtani, E. (2017) Single crystal synthesis of δ-(Al,Fe)OOH. American Mineralogist, 102(9), 1953-1956.

Klotz, S., Chervin, J.C., Munsch, P., and Le Marchand, G. (2009) Hydrostatic limits of 11 pressure transmitting media. Journal of Physics D: Applied Physics, 42(7), 075413.

Lavina, B., Dera, P., Downs, R.T., Prakapenka, V., Rivers, M., Sutton, S., and Nicol, M. (2009) Siderite at lower mantle conditions and the effects of the pressure-induced spin-pairing transition. Geophysical Research Letters, 36(23), L23306.

Li, S., Ahuja, R., and Johansson, B. (2006) The elastic and optical properties of the high-pressure hydrous phase δ-AlOOH. Solid State Communications, 137(1-2), 101-106.

Lin, J.-F., Liu, J., Jacobs, C., and Prakapenka, V.B. (2012) Vibrational and elastic properties of ferromagnesite across the electronic spin-pairing transition of iron. American Mineralogist, 97(4), 583-591.

Lin, J.-F., Speziale, S., Prakapenka, V.B., Dera, P., Lavina, B., and Watson, H.C. (2010) High-pressure X-ray diffraction and X-ray emission studies on iron-bearing silicate perovskite under high pressures. High Pressure Research, 30(2), 230-237.

Lin, J.-F., Struzhkin, V.V., Jacobsen, S.D., Hu, M.Y., Chow, P., Kung, J., Liu, H., Mao, H.K., and Hemley, R.J. (2005) Spin transition of iron in magnesiowustite in the Earth's lower mantle. Nature, 436(7049), 377-80.

Liu, J., Caracas, R., Fan, D., Bobocioiu, E., Zhang, D., and Mao, W.L. (2016) High-pressure compressibility and vibrational properties of $(Ca,Mn)CO_3$. American Mineralogist, 101(12), 2723-2730.

Liu, J., Hu, Q., Bi, W., Yang, L., Xiao, Y., Chow, P., Meng, Y., Prakapenka, V.B., Mao, H.K., and Mao, W.L. (2019)

Altered chemistry of oxygen and iron under deep Earth conditions. Nature Communications, 10(1), 153.

Liu, J., Hu, Q., Young Kim, D., Wu, Z., Wang, W., Xiao, Y., Chow, P., Meng, Y., Prakapenka, V.B., Mao, H.K., and Mao, W.L. (2017) Hydrogen-bearing iron peroxide and the origin of ultralow-velocity zones. Nature, 551(7681), 494-497.

Liu, J., Lin, J.F., Mao, Z., and Prakapenka, V.B. (2014) Thermal equation of state and spin transition of magnesiosiderite at high pressure and temperature. American Mineralogist, 99(1), 84-93.

Liu, J., Wang, C., Lv, C., Su, X., Tang, R., Chen, J., Hu, Q., Mao, H.-K., and Mao, L.W. (2020) Evidence for oxygenation of Fe-Mg oxides at mid-mantle conditions and the rise of deep oxygen. National Science Review, in press.

Lobanov, S.S., Goncharov, A.F., and Litasov, K.D. (2015) Optical properties of siderite ($FeCO_3$) across the spin transition: Crossover to iron-rich carbonates in the lower mantle. American Mineralogist, 100(5-6), 1059-1064.

Mao, H.-K., and Mao, W.L. (2020) Key problems of the four-dimensional Earth system. Matter and Radiation at Extremes, 5(3), 038102.

Mao, H., Xu, J.-A., and Bell, P. (1986) Calibration of the ruby pressure gauge to 800 kbar under quasi-hydrostatic conditions. Journal of Geophysical Research: Solid Earth, 91(B5), 4673-4676.

Mashino, I., Murakami, M., and Ohtani, E. (2016) Sound velocities of δ-AlOOH up to core-mantle boundary pressures with implications for the seismic anomalies in the deep mantle. Journal of Geophysical Research: Solid Earth, 121(2), 595-609.

Mattila, A., Pylkkänen, T., Rueff, J.P., Huotari, S., Vankó, G., Hanfland, M., Lehtinen, M., and Hämäläinen, K. (2007) Pressure induced magnetic transition in siderite $FeCO_3$ studied by x-ray emission spectroscopy. Journal of Physics: Condensed Matter, 19(38), 386206.

Ohira, I., Jackson, J.M., Solomatova, N.V., Sturhahn, W., Finkelstein, G.J., Kamada, S., Kawazoe, T., Maeda, F., Hirao, N., Nakano, S., Toellner, T.S., Suzuki, A., and Ohtani, E. (2019) Compressional behavior and spin state of δ-(Al,Fe)OOH at high pressures. American Mineralogist, 104(9), 1273-1284.

Ohira, I., Ohtani, E., Sakai, T., Miyahara, M., Hirao, N., Ohishi, Y., and Nishijima, M. (2014) Stability of a hydrous δ-phase, $AlOOH–MgSiO_2(OH)_2$, and a mechanism for water transport into the base of lower mantle. Earth and Planetary Science Letters, 401, 12-17.

Ohtani, E. (2005) Water in the Mantle. Elements, 1(1), 25-30.

Ohtani, E. (2020) The role of water in Earth's mantle. National Science Review, 7(1), 224-232.

Ohtani, E., Litasov, K., Suzuki, A., and Kondo, T. (2001) Stability field of new hydrous phase, δ-AlOOH, with implications for water transport into the deep mantle. Geophysical Research Letters, 28(20), 3991-3993.

Sano-Furukawa, A., Hattori, T., Komatsu, K., Kagi, H., Nagai, T., Molaison, J.J., Dos Santos, A.M., and Tulk, C.A. (2018) Direct observation of symmetrization of hydrogen bond in delta-AlOOH under mantle conditions using neutron diffraction. Scientific Reports, 8(1), 15520.

Sano-Furukawa, A., Kagi, H., Nagai, T., Nakano, S., Fukura, S., Ushijima, D., Iizuka, R., Ohtani, E., and Yagi, T. (2009) Change in compressibility of δ-AlOOH and δ-AlOOD at high pressure: A study of isotope effect and hydrogen-bond symmetrization. American Mineralogist, 94(8-9), 1255-1261.

Sano, A., Ohtani, E., Kondo, T., Hirao, N., Sakai, T., Sata, N., Ohishi, Y., and Kikegawa, T. (2008) Aluminous hydrous mineral δ-AlOOH as a carrier of hydrogen into the core-mantle boundary. Geophysical Research Letters, 35(3), L03303.

Su, X.W., Zhao, C.S., Lv, C.J., Zhuang, Y.K., Salke, N., Xu, L.X., Tang, H., Gou, H.Y., Yu, X.H., Sun, Q., Liu, J., The effect of iron on the sound velocities of δ-AlOOH up to 135 GPa, Geoscience Frontiers, in press.

Thompson, E.C., Campbell, A.J., and Tsuchiya, J. (2017) Elasticity of ε-FeOOH: Seismic implications for Earth's

lower mantle. Journal of Geophysical Research: Solid Earth, 122(7), 5038-5047.

Thompson, E.C., Davis, A. H., Brauser, N. M., Liu, Z. X., Prakapenka, V. B., and Campbell, A.J. (2020) Phase transitions in ε-FeOOH at high pressure and ambient temperature. American Mineralogist, in press.Tsuchiya, J., and Tsuchiya, T. (2009) Elastic properties of δ-AlOOH under pressure: First principles investigation. Physics of the Earth and Planetary Interiors, 174(1-4), 122-127.

Tsuchiya, J., Tsuchiya, T., and Wentzcovitch, R.M. (2008) Vibrational properties of δ-AlOOH under pressure. American Mineralogist, 93(2-3), 477-482.

Williams, Q., Collerson, B., and Knittle, E. (1992) Vibrational spectra of magnesite ($MgCO_3$) and calcite-III at high pressures. American Mineralogist, 77(11-12), 1158-1165.

Yuan, H., Zhang, L., Ohtani, E., Meng, Y., Greenberg, E., and Prakapenka, V.B. (2019) Stability of Fe-bearing hydrous phases and element partitioning in the system $MgO–Al_2O_3–Fe_2O_3–SiO_2–H_2O$ in Earth's lowermost mantle. Earth and Planetary Science Letters, 524, 115714.

Zhang, L., Yuan, H., Meng, Y., and Mao, H.K. (2018) Discovery of a hexagonal ultradense hydrous phase in (Fe,Al)OOH. Proceedings of the National Academy of Sciences of the United States of America, 115(12), 2908-2911.

Zhuang, Y., Cui, Z., Zhang, D., Liu, J., Tao, R., and Hu, Q. (2019) Experimental Evidence for Partially Dehydrogenated ε-FeOOH. Crystals, 9(7), 356.